Atmos. Chem. Phys. Discuss., 14, 11447–11491, 2014
www.atmos-chem-phys-discuss.net/14/11447/2014/
doi:10.5194/acpd-14-11447-2014

Atmospheric Chemistry and Physics Discussions

Size-resolved observations of refractory black carbon particles in cloud droplets at a marine boundary layer site

J. C. Schroder[1], S. J. Hanna[1], R. L. Modini[2], A. L. Corrigan[2], A. M. Macdonald[3], K. J. Noone[5], L. M. Russell[2], W. R. Leaitch[4], and A. K. Bertram[1]

[1]Department of Chemistry, University of British Columbia, Vancouver, BC, V6T 1Z1, Canada
[2]Scripps Institute of Oceanography, University of California-San Diego, La Jolla, CA, USA
[3]Air Quality Processes Research Section, Environment Canada, Toronto, Ontario, Canada
[4]Climate Chemistry and Measurements Research, Environment Canada, Toronto, Ontario, Canada
[5]Department of Applied Environmental Science, Stockholm University, Stockholm, Sweden

Received: 4 April 2014 – Accepted: 23 April 2014 – Published: 7 May 2014

Correspondence to: A. K. Bertram (bertram@chem.ubc.ca)

Published by Copernicus Publications on behalf of the European Geosciences Union.

Abstract

Size resolved observations of aerosol particles (including black carbon particles) and cloud residuals were studied at a marine boundary layer site (251 m a.m.s.l.) in La Jolla, CA during 2012. A counterflow virtual impactor was used to sample cloud residuals while a total inlet was used to sample both cloud residuals and interstitial particles. Two cloud events totaling ten hours of in-cloud sampling were analyzed. Since the CVI only sampled cloud droplets larger than ≈ 11 µm, less than 100 % of the cloud droplets were sampled during the two cloud events (≈ 38 % of the cloud droplets for the first cloud event and ≈ 24 % of the cloud droplets for the second cloud were sampled). Back trajectories showed that air masses for both cloud events spent at least 96 h over the Pacific Ocean and traveled near, or over populated regions just before sampling. Based on bulk aerosol particle concentrations measured from the total inlet the two air masses sampled were classified as polluted marine air, a classification that was consistent with back trajectory analysis and the mass concentrations of refractory black carbon (rBC) measured from the total inlet. The activated fraction of rBC, estimated from the measurements, ranged from 0.01 to 0.1 for core diameters ranging from 70 to 220 nm. Since the fraction of cloud droplets sampled by the CVI was less than 100 %, the measured activated fractions of rBC should be considered as lower limits to the total fraction of rBC activated during the two cloud events. Size distributions of rBC sampled from the residual inlet show that sub-100 nm rBC cores were incorporated into the droplets in both clouds. The coating analysis shows that the rBC cores had average coating thicknesses of 75 nm for core diameters of 70 nm and 29 nm for core diameters of 220 nm. The presence of sub-100 nm rBC cores in the cloud residuals is consistent with kappa-Köhler theory and the measured coating thicknesses of the rBC cores.

ACPD
14, 11447–11491, 2014

1 Introduction

Black carbon (BC) particles, which typically have sizes less than 1 µm, are emitted into the atmosphere through incomplete combustion of fossil fuels or biomass burning (Bond et al., 2013). When first emitted into the atmosphere these particles are thought to mainly be hydrophobic. During their atmospheric lifecycle hydrophilic substances, such as sulfate or water soluble organics, can form a coating surrounding the black carbon cores (Ching et al., 2012; Metcalf et al., 2012; Schwarz et al., 2008b), enabling the particles to act as cloud condensation nuclei (CCN). Modeling studies have shown that this process can occur in the boundary layer on the order of hours during the daytime (Riemer et al., 2004, 2010).

By absorbing solar radiation or by acting as CCN, BC particles can influence climate both directly and indirectly (Bond et al., 2013; Wang, 2013; Wang et al., 2013; Zhuang et al., 2010). To predict both the direct and indirect effects of black carbon on climate, a good understanding of the CCN ability of BC is needed (Koch et al., 2011; Vignati et al., 2010; Wang, 2013). When describing the CCN properties of black carbon in atmospheric models, different approaches have been applied. Often BC is intially assumed to be CCN inactive and converted to a CCN active species after a prescribed time and at a constant efficiency (Koch et al., 2011; Vignati et al., 2010; Wang, 2013). Alternatively, the CCN properties of particles containing BC in models have been described by Köhler theory (Ching et al., 2012; Jacobson, 2012; Koch et al., 2011; Riemer et al., 2010).

The CCN ability of BC particles has been studied in both laboratory and field studies (Cozic et al., 2007; Dusek et al., 2011; Hallberg et al., 1992, 1994; Henning et al., 2010, 2012; Hitzenberger et al., 2000, 2001; Kasper-Giebl et al., 2000; Koehler et al., 2009; Kuwata et al., 2009; Noone et al., 1992; Petters et al., 2009; Petzold et al., 2005; Popovicheva et al., 2011; Sellegri et al., 2003; Verheggen et al., 2007). Laboratory studies have examined both coated and uncoated black carbon particles (Dusek et al., 2011; Henning et al., 2010, 2012; Koehler et al., 2009; Petters et al., 2009; Petzold

ACPD
14, 11447–11491, 2014

et al., 2005; Popovicheva et al., 2011). These studies have shown that for uncoated flame or spark generated BC the particles are not activated into cloud droplets even with supersaturations of $\geq 1\,\%$ (Henning et al., 2012). On the other hand, once BC is coated with hygroscopic material the supersaturation required for activation is significantly deacreased, a decrease that can be described under laboratory conditions by Köhler theory (Henning et al., 2010, 2012; Petzold et al., 2005; Popovicheva et al., 2011). Field measurements of the activated fraction of BC in cloud droplets have also investigated the CCN ability of BC particles. Most measurements have shown that as BC particles age in the atmosphere the fraction incorporated into cloud droplets increases (Cozic et al., 2007; Hitzenberger et al., 2000, 2001; Kasper-Giebl et al., 2000; Sellegri et al., 2003; Verheggen et al., 2007). An exception to this trend is the work done by Granat et al. (2010) which showed that after several days of travel in the winter subtropical marine environment, soot retained much of its hydrophobic properties. Some field studies (Hallberg et al., 1992, 1994) have shown that 10–20 % of atmospheric BC can activate at supersaturations of between ≈ 0.2–$0.5\,\%$.

Although the activated fraction of BC in cloud droplets have been measured at some locations, the true contribution of BC to CCN in the atmosphere is unknown, yet potentially significant (Chen et al., 2010). Measurements of the activated fraction of BC as a function of size are important to test our current understanding of the incorporation of BC particles into cloud droplets. In this study we measured BC as a function of size in cloud residuals at a marine boundary layer site (251 m a.m.s.l.) in La Jolla, CA during 2012 and compared the results with BC as a function of size measured from a total inlet that sampled both cloud residuals and interstitial particles. Coating thicknesses of BC cores in the cloud residuals were also determined. The measurements of BC as a function of size in cloud residuals were further compared to predictions with kappa-Köhler theory.

ACPD
14, 11447–11491, 2014

2 Site, sampling and analysis

2.1 Site description

The sampling site was located below the peak of Mt. Soledad (251 m a.m.s.l.), which is 3 km from the coast of the Pacific Ocean in La Jolla, CA (32.8400° N, 117.2769° W). The city of La Jolla is predominately residential with a population of approximately 43 000 people and situated 24 km north of San Diego (population 1.3 million), the closest urban center.

Data were collected from 27 May to 18 June 2012 using instruments housed in a modified shipping container. A total of three clouds were sampled during this time frame. The first cloud event was rejected from analysis due to an instrumental error. The second cloud event occurred from 12 June 2012 20:43 to 13 June 2012 11:35 PDT, and hereinafter called Cloud 2. The third cloud event took place from 17 June 2012 20:36 to 18 June 2012 07:52 PDT, and called Cloud 3 for the remainder of the document.

2.2 Inlets

Two inlets, referred to as the total inlet and residual inlet, were used during this study (Fig. 1). The total inlet measured both interstitial and cloud residual particles during cloud events. This heated inlet was designed and built following the specifications reported by Bates et al. (2002) and therefore assumed to have the same transmission efficiency, namely > 95 % for particles < 6.5 µm.

The intake of the residual inlet was a counterflow virtual impactor (CVI, see Sect. 2.3 and Appendix A) that enabled the sampling of cloud droplets without interstitial particles, thus only the residual particles of the cloud droplets were sampled. This inlet was used only during cloudy periods and was connected to a branch of the total inlet by a 3-way valve (Fig. 1). During a cloud event, the valve was manually switched so that cloud droplets were sampled through the CVI and cloud residuals were measured

ACPD
14, 11447–11491, 2014

by instrumentation connected downstream of the valve. At times when no clouds were present the valve was switched such that all instruments sampled ambient particles.

Since much of the analysis performed in this study is based on a measured ratio of particle number concentration it was necessary to ensure that there were no significant losses of particles due to the inlet configuration. Therefore, particle losses from diffusion, sedimentation, turbulent inertial deposition and inertial deposition from both bends and contractions for the total and residual inlets (assuming cloud free sampling) were calculated using the Particle Loss Calculator (Von der Weiden et al., 2009) and found to be $< 2\,\%$ for particles with diameters between 0.07 and 1 µm, covering the size range used for this analysis.

2.3 Counterflow virtual impactor sampling

The CVI was based on the design by Noone et al. (1988), where droplet laden air was drawn into the CVI using a high velocity air intake vacuum ($\approx 92\,\mathrm{m\,s^{-1}}$). Only those droplets with enough inertia to overcome a counterflow of zero-air with an average flow rate of ≈ 5 LPM made it past the region known as the stagnation plane and were therefore transported to the instruments downstream. Water from these droplets began evaporating upon impact with the warm dry counterflow, held at a constant temperature of 40 °C, and particles were further dried by a heated section of the sampling tube, also at 40 °C, leaving only the droplet residuals to be sampled downstream. If the droplets were completely evaporated, any volatile gases in the cloud droplets, such as nitric acid, likely evaporated and were not part of the residual particles (Zhao et al., 2014). If some water was retained by the residual particles at this temperature, a fraction of highly soluble volatile components may have also remained.

The smallest droplet diameter for which 50 % of the particles are sampled is considered to be the CVI cut-size (CVI – D_{50}) and is the diameter for which a droplet's stopping distance is greater than the CVI inlet diameter and the length to the end of the stagnation plane (Anderson et al., 1993; Noone et al., 1988). For the clouds sampled

ACPD
14, 11447–11491, 2014

in this study a CVI – D_{50} of 11.5 ± 0.7 µm and 11.6 ± 0.7 µm for Cloud 2 and Cloud 3, respectively, were calculated (see Appendix A for details).

Due to the properties of a CVI, particle concentrations are enhanced at the exit of the CVI compared to ambient conditions. Enhancement factors (EF) of 7.1 and 7.4 for Cloud 2 and Cloud 3, respectively, were calculated based on the flow rates used during sampling (Appendix A).

2.4 Refractory black carbon mass measurements

Refractory black carbon (rBC) mass was measured from the total inlet and the residual inlet using two separate single particle soot photometers (SP2, DMT, Boulder, CO). These instruments are referred to as the total SP2 ($SP2_{Tot}$) and the residual SP2 ($SP2_{Res}$). The location of these instruments is shown in Fig. 1. The SP2 has been described in detail elsewhere (Moteki and Kondo, 2007; Schwarz et al., 2006; Stephens et al., 2003). Briefly, particles are sampled at ≈ 0.12 LPM and carried directly into a chamber housing a high intensity (≈ 1 MW cm^{-2}) intra-cavity Nd:YAG laser operating at λ = 1064 nm. BC particles are rapidly heated, through absorption, to incandescence, where the emitted visible light is detected by two photomultipliers. The mass of individual rBC particles can be determined using a calibration plot, where the amplitude of the detector response is proportional to the mass of a reference material. The two SP2s used in this study were calibrated pre and post-campaign with Aquadag® (Moteki et al., 2009), using effective densities reported by Gysel et al. (2011). The calibration parameters used to determine mass were taken from a second order polynomial fit of the combined pre and post-campaign data. A volume equivalent diameter was also determined from the measured mass assuming a black carbon density of 1.8 g cm^{-3} (Bond and Bergstrom, 2006). The $SP2_{Res}$ was a 4 channel instrument with a detection range of 70–220 nm, whereas the $SP2_{Tot}$ was an 8 channel instrument with a detection range of 70–558 nm.

ACPD
14, 11447–11491, 2014

2.5 Refractory black carbon coating thickness measurements

In addition to measuring the incandescence signal, the SP2 measured the elastically scattered light from rBC and non-rBC containing particles with two avalanche photodiodes (APDs). Both APDs were set to the high gain setting for collection, and one of the APDs was a split detector. The APDs generate a time dependent signal as particles pass through the Gaussian laser beam. The split detector APD is used to obtain position information, whereas the APD without the split detector is used to obtain information on the elastic scattering intensity from particles (Gao et al., 2007). The signal from the non-split detector was calibrated using polystyrene latex beads (PSL) particles (200 and 300 nm in diameter). This gives a calibration curve that relates the amplitude of the measured scattering signal to the scattering intensity determined from a Mie calculation. These Mie calculations involved calculating the scattering intensity for each PSL size over the solid angle of the SP2 detector (a full-angle cone of 65° at 45° and 135° from the laser axis, Gao et al., 2007; Schwarz et al., 2008b) using a Mie code (Leinonen) based on that of Mätzler (2002a, b). The refractive index used for the PSL Mie calculations was $1.59 - 0.0i$.

The information from the two APDs was used to determine the coating thicknesses on rBC cores as described by Gao et al. (2007). Due to a failure of the split detector on the SP2 connected to the total inlet, coating thicknesses on rBC cores were only determined from the data collected with the SP2 connected to the residual inlet. To determine coating thicknesses the scattering amplitudes for rBC containing particles were determined using the leading-edge only (LEO) fitting method (Gao et al., 2007). In short, the early part of the elastic scattering signal (up to 5 % of the maximum laser intensity, Gao et al., 2007) was fit to a Gaussian function and the maximum scattering amplitude was retrieved from the fit. Parameters included in the curve fitting were the peak position and full width at half maximum, determined with the positional information from the split detector and calibration measurements with PSL particles prior to the field campaign.

ACPD
14, 11447–11491, 2014

Since the mass of the rBC core is known from the incandescence signal and the maximum scattering amplitude is determined from the leading-edge analysis, a core-shell Mie model can be employed to determine what coating thickness would give the measured scattering signal for that particular particle (Gao et al., 2007; Schwarz et al., 2008b). In this work a core-shell Mie model was used to construct a lookup table for core diameters of 60 to 220 nm (in 1 nm increments) and shell thicknesses from 0 to 360 nm (in 1 nm increments). The complex index of refraction used for the core was $1.95 - 0.79i$ (Bond and Bergstrom, 2006) and for the shell was $1.5 - 0.0i$, which is consistent with that of dry sulfate or sodium chloride (Metcalf et al., 2012; Schwarz et al., 2008a, b). The PSL calibration was used to scale all calculated values to measured values. The elastic scattering amplitudes and the rBC core diameters were then used with this lookup table to determine coating thicknesses for each rBC containing particle.

As mentioned above, only data collected with the SP2 connected to the residual inlet was analyzed for coating thickness. Approximately 99 % of the rBC containing particles detected with the $SP2_{Res}$ had elastic scattering signals above the background signals on the APDs. Nevertheless, only 50 % of the rBC containing particles detected with the $SP2_{Res}$ were successfully fit with the LEO fitting procedure. Hence, coating information reported here is only from a subset of the rBC particles measured with the $SP2_{Res}$. Failure to fit the elastic scattering signals with the LEO procedure was mainly due to either; (a) large scattering signals that saturated the APD detector, or (b) time dependent scattering signals were above 5 % of the maximum laser intensity at time zero. 11 % and 27 % of all rBC containing particles detected with the $SP2_{Res}$ had a failure due to (a) and (b), respectively.

2.6 Size distribution measurements of the bulk aerosol

Two instruments were used to measure particle size distributions (Fig. 1). Size distributions of particles sampled from the total inlet were determined with a scanning electrical mobility spectrometer (SEMS, model 2002, BMI, Hayward, CA), which counted parti-

ACPD
14, 11447–11491, 2014

cles into 61 discrete size bins from 0.01–1 µm with a 5 min scan time interval. Size distributions of particles sampled from the residual inlet were determined with a scanning mobility particle sizer (SMPS, model 3034, TSI, St. Paul, MN), which recorded particle counts into 55 size bins from 10–487 nm with a 3 min scan time interval. Both the SEMS and SMPS operate based on the coupling of a size selecting differential mobility analyzer and a condensational growth particle counter. During cloud free sampling the SMPS and SEMS agreed to within 4 % for particles between 70 and 400 nm.

2.7 Aerosol mass spectrometry

An online high-resolution aerosol mass spectrometer (HR-ToF-AMS, Aerodyne Research Inc., Billerica, MA) was operated downstream of the CVI on the residual inlet to characterize the chemical composition of the cloud droplet residuals. The HR-ToF-AMS measured non-refractory, sub-micrometer aerosol chemical composition at high time resolution (DeCarlo and Kimmel, 2006). Here we only consider data measured by the HR-ToF-AMS in its mass-spectrum and V-modes of operation. These data were recorded as 2 min averages every 4–6 min, depending on how many other modes of operation (W-mode, light scattering) the instrument was alternating between. Size-resolved composition data for the residual particles measured by the HR-ToF-AMS in time-of-flight mode are not considered here since the signal was generally at or below the detection limit. Standard quantification procedures (Allan et al., 2004) were applied to the mass spectra measured by the HR-ToF-AMS to determine the relative concentrations of the non-refractory species (organic, nitrate, sulfate, ammonium and chloride) typically reported by aerosol mass spectrometry.

2.8 Back trajectories

Air mass back trajectories were calculated using the NOAA Hybrid Single Particle Lagrangian Integrated Trajectory Model (HYSPLIT) (Draxler and Rolph, 2013; Rolph, 2013). All trajectory calculations used the National Centers for Environmental Predic-

ACPD
14, 11447–11491, 2014

tions EDAS meteorological dataset. Trajectories were calculated starting at 10 m a.g.l., 96 h backwards in time, and at hourly intervals throughout the entire period of cloud sampling.

2.9 Cloud properties

A fog monitor (FM-100, model 100, DMT, Boulder, CO), which is a forward scattering optical spectrometer, was stationed on top of the container providing an in-situ measurement of cloud droplet number concentration (CDNC) in 20 discrete size bins ranging from 2–50 µm, whilst simultaneously monitoring the liquid water content (LWC) present with a 1 s time resolution (Eugster et al., 2006).

3 Results and discussion

3.1 Back trajectories

The back trajectories for Cloud 2 (Fig. 2a and c) show that the air mass spent most of the previous 96 h over the Pacific Ocean and arrived at the sampling site from a northwesterly direction. During the first part of Cloud 2 (12 June 21:00 to 13 June 08:00 PDT) the back trajectories became progressively more northerly and the air mass began traveling near large populated urban regions. Towards the end of the cloud event (at ≈ 09:00 PDT on 13 June) the winds shifted to southwesterly. Based on the back trajectories the air mass for Cloud 2 traveled ≈ 40–50 km over land before reaching the sampling site. In addition, the air mass spent a significant amount of time close to the ocean surface prior to being lifted up to the sampling site (Fig. 2c).

The back trajectories for Cloud 3 (Fig. 2b and d) also show that the air mass spent the majority of the previous 96 h over the Pacific Ocean before arriving at the site. At the start of Cloud 3 (17 June 21:00 to 22:00 PDT) the air mass arrived from the northwest. Throughout the remainder of the cloud event (17 June 23:00 to 18 June 08:00 PDT) the air mass continued to shift farther north and by the end of the cloud

ACPD
14, 11447–11491, 2014

event (18 June 08:00 PDT) the air mass was traveling south along the coastline before arriving at the sampling site. The back trajectories indicate that the air mass traveled ≈ 10–20 km over land prior to arriving at the sampling site. Similar to Cloud 2, the air spent a significant amount of time close to the ocean surface prior to being lifted up to the sampling location (Fig. 2d). Since the trajectories during both clouds are close to the coastline for a period of time, it is likely these air masses contained both marine particles and anthropogenic emissions.

3.2 Meteorological conditions and cloud properties

For the purposes of this study, the data were classified as in-cloud and included for analysis if they met the following criteria: (1) the five minute averaged CVI counterflow was within $\pm 5\sigma$ of the mean counterflow to ensure only periods of stable CVI flows were included; and (2) the five minute averaged LWC was greater than 0.05 g m^{-3} to remove periods of entrainment, or "patchy" regions of the cloud as much as possible (Cozic et al., 2007).

The measured cloud properties as a function of time are shown in Fig. 3a–c, where Cloud 2 is shown on the left side and Cloud 3 is shown on the right side of the plot. Cloud 2 was characterized by an average temperature of 13.4 ± 0.2 °C with light and variable winds (0.5 ± 0.2 m s^{-1} and 190 ± 90° respectively), and an average LWC of 0.13 ± 0.07 g m^{-3}. During the middle portion of Cloud 2 (13 June 01:00 to 02:00 PDT) the droplet distributions clearly show an interval where the number of droplets above the CVI – D_{50} (black trace overlaid on panel C) increases significantly, which coincides, in time, with a sharp increase in LWC. Cloud 3 was characterized by an average temperature of 15.2 ± 0.1 °C, northerly (330 ± 10°) winds with an average speed of 1.5 ± 0.4 m s^{-1}, and an average LWC of 0.09 ± 0.02 g m^{-3}.

The cloud droplet number and volume size distributions, averaged over the entire event, are shown in Fig. 4, and further summarized in Table 1. Cloud 3 had a CDNC of 146 cm^{-3}, a factor of two higher than during Cloud 2 (68 cm^{-3}).

ACPD
14, 11447–11491, 2014

From the calculated CVI – D_{50} and the fits to the droplet size distribution (Fig. 4) the number and volume fraction of droplets sampled by the CVI were determined. The results are summarized in Table 1. During Cloud 2 the number fraction of droplets larger than the CVI – D_{50} was about 38 % and for Cloud 3 the fraction sampled was about 24 %. Since only the larger droplets were sampled by the CVI during these two cloud events, the results presented herein are only representative of the larger droplet population.

3.3 Size distributions

Average size distributions of the bulk aerosol particles and rBC particles measured from the total and residual inlets for both Cloud 2 and Cloud 3 are shown in Fig. 5. Data are plotted in two ways: on a log scale, in panels A and B, and normalized to the respective maximum, in panels C and D. Table 2 summarizes the results obtained from the size distribution analysis.

3.3.1 Size distributions measured from the total inlet ($\text{BulkAero}_{\text{Tot}}$ and rBC_{Tot})

The average size distributions of the bulk aerosol measured from the total inlet (referred to as $\text{BulkAero}_{\text{Tot}}$ for the remainder of the document) and the average size distributions of the refractory black carbon measured from the total inlet (referred to as rBC_{Tot} for the remainder of the document) are shown in Fig. 5. The $\text{BulkAero}_{\text{Tot}}$ distributions for both clouds show evidence of at least two overlapping modes. A single mode lognormal distribution function was fit to the data yielding mean geometric diameters (D_g) of 108 and 81 nm with geometric standard deviations (σ_g) of 1.58 and 1.70 for Cloud 2 and Cloud 3 respectively. Integration of the number distribution during Cloud 2 results in a total number concentration (N_{Tot}) for the bulk aerosol of 981 cm^{-3}. Likewise, N_{Tot} during Cloud 3 was measured to be 994 cm^{-3}. Previous measurements in the marine boundary layer have classified the environment as "clean" marine if the number of particles is $\leq$ 300–500 cm^{-3} and "polluted" marine if the number concentrations are

ACPD
14, 11447–11491, 2014

≥ 400–1500 cm^{-3} (Andreae, 2009; Bates et al., 2000; O'Dowd et al., 2001; Glantz and Noone, 2000; Hawkins et al., 2010; Pirjola and O'Dowd, 2000; Twohy et al., 2005). Thus the particle concentrations measured at Mt. Soledad, in addition to the back trajectories, suggest that for both clouds the air masses can be classified as polluted marine aerosols. The size distributions of the $BulkAero_{Tot}$ as a function of time are also included in Fig. 3d for comparison.

The rBC_{Tot} size distributions for each cloud are shown in Fig. 5. The D_g for rBC_{Tot} (assuming the number distributions are lognormal) during both events lies somewhere in the nucleation mode at < 70 nm, which is outside the detection range of the SP2. Integration of the rBC_{Tot} distributions, from 70–220 nm, yields and N_{Tot} of 75 cm^{-3} during Cloud 2 and 62 cm^{-3} in Cloud 3. Assuming a BC density of 1.8 $g\,cm^{-3}$ the total mass concentration (M_{Tot}) are 73 and 62 $ng\,m^{-3}$ for Cloud 2 and Cloud 3 respectively (Table 2). The rBC_{Tot} mass concentrations observed at Mt. Soledad were higher than concentrations measured in clean marine air (Cooke, 1997; Shank et al., 2012), but considerably lower than concentrations measured in most urban environments (see Table 1 in Metcalf et al., 2012).

3.3.2 Size distributions measured from the residual inlet ($BulkAero_{Res}$ and rBC_{Res})

Average size distributions of the bulk aerosol measured from the residual inlet (referred to as $BulkAero_{Res}$ for the remainder of the document) are also shown in Fig. 5. The size distributions of the $BulkAero_{Res}$ indicate that it was mostly the larger particles of the $BulkAero_{Tot}$ distributions that were incorporated into the sampled cloud droplets. The size distributions of $BulkAero_{Res}$ as a function of time for both cloud events are included in Fig. 3e for comparison.

The size distributions for $BulkAero_{Res}$ shown in Fig. 5 have a local minimum at 110 nm for Cloud 2 and 90 nm for Cloud 3. The particles observed at sizes less than

ACPD
14, 11447–11491, 2014

the local minima may be due to droplet "splash", or due to a leak in the CVI. (Pekour and Cziczo, 2011; Schwarzenboeck et al., 2000; Vidaurre et al., 2011).

Figure 5 also shows the size distributions of the rBC residuals measured with the CVI. Figure 5 shows that rBC cores smaller than 100 nm are incorporated into cloud droplets. In addition, Fig. 5 shows that most of the rBC_{Res} have effective sizes of less than 100 nm and that the rBC_{Res} are overall larger than the rBC_{Tot}. Fitting the rBC_{Res} size distributions (assuming these distributions are lognormal) results in mean geometric diameters of 87 and 81 nm for Clouds 2 and 3 respectively.

3.4 Size-resolved activated fraction

The size-resolved activated fraction [$AF(D_p)$] for rBC and the bulk aerosol were calculated by taking the ratio of the number size distributions measured from the residual inlet and the number size distributions measured from the total inlet. Prior to calculating $AF(D_p)$, a spline interpolation algorithm was applied to the rBC and bulk aerosol number size distributions. After a spline interpolation was applied to the data, the following equation was used to calculate the size-resolved activated fraction:

$$AF(D_p) = \frac{N_{Res}(D_p) \cdot CF(D_p)}{N_{Tot}(D_p) \cdot EF \cdot DT} \quad (1)$$

where $N_{Res}(D_p)$ is the number of residual particles as a function of size, $CF(D_p)$ is the size-resolved instrument sensitivity correction factor, $N_{Tot}(D_p)$ is the number of particles measured from the total inlet as a function of size, EF is the CVI enhancement factor (see Appendix A) and DT is the droplet transmission factor through the CVI. Calculations of the droplet transmission factor are given in Appendix C and plotted in Fig. A1. $CF(D_p)$, which corrects for variances in instrument detection efficiencies, were determined from a 12 h period of cloud free air on 5 June 2012 for the bulk aerosol and from side by side ambient sampling of room air during the post-campaign calibration for rBC.

ACPD
14, 11447–11491, 2014

The AF(D_p) for the bulk aerosol and rBC are presented in Fig. 6, where the error bars represent one standard deviation (1σ) of the AF for each 10 nm size bin. The AF as a function of size for the bulk aerosol is similar to previous measurements in similar clouds (Hallberg et al., 1994). Figure 6a and b show that the AF of rBC cores is significant, even for core diameters of $\leq$ 100 nm. Figure 6a and b also show that during both clouds the AF for rBC cores is larger than the AF for the bulk aerosol at diameters $<\approx$150 nm. These results can be explained by the presence of large coatings surrounding the core (see Sect. 3.5). Since the fraction of droplets sampled by the CVI was < 100 %, the calculated AF should be considered as a lower limit to the total fraction activated during these two cloud events.

3.5 Coating thickness of rBC residuals

Coating thicknesses were determined using a core and shell Mie model and are shown in Fig. 6c and d, where the error bars represent 1σ and the symbols represent the averages. When calculating coating thicknesses, the particles were idealized as a pure BC core uniformly coated with a non-absorbing material, although the actual particle morphology may be more complicated (Sedlacek et al., 2012). As mentioned in Sect. 2.5, only 50 % of the rBC containing particles detected with the $SP2_{Res}$ were successfully fit with the LEO fitting procedure. Hence, coating information reported below is only from a subset of the rBC residual particles measured.

Both cloud events show a similar trend, namely that the coating thicknesses are larger at smaller rBC core diameters than larger rBC core diameters, which has also been observed elsewhere (Metcalf et al., 2012). At small core diameters (70–100 nm) the coating thicknesses range from roughly 45–115 nm, while at larger core diameters (200–215 nm) the coatings range from roughly 0–60 nm. Coating thicknesses measured in this study fall between values measured in previous studies. For example, coating thicknesses ranging from 20 $\pm$ 10 nm, in fresh urban plumes (Schwarz et al., 2008a), up to 188 $\pm$ 31 nm on more aged rBC particles (Metcalf et al., 2012) have been reported.

ACPD
14, 11447–11491, 2014

3.6 Size distributions of rBC_{Res}(Core+Coating)

For rBC particles measured from the residual inlet, a core diameter (determined from the incandescence signal) and a coating thickness (determined from the Mie scattering calculations discussed in Sect. 2.5) were combined to calculate the overall rBC particle diameter (Core + Coating). These data are plotted in Fig. 7, where the distributions are shown to be shifted to larger sizes when compared with the distributions plotted as a function of core diameter [rBC_{Res}(Core)] alone. Furthermore, incorporating the coating into the rBC size distributions result in greater similarities with the size distributions of the bulk aerosol.

3.7 Comparison of rBC_{Res} as a function of size with predictions based on kappa-Köhler theory

Sections 3.4 and 3.5 provide a qualitative explanation for why rBC cores smaller than 100 nm are incorporated into cloud droplets – the rBC cores have thick coatings which lead to overall particle diameters > 100 nm. In the following, we expand on this qualitative explanation by carrying out a quantitative analysis showing that the presence of rBC cores smaller than 100 nm in the cloud residuals is consistent with kappa–Köhler theory. This quatitative analysis consists of the following steps: (1) an estimation of the bulk aerosol composition; (2) an estimation of the critical diameter for activation of the cloud droplets sampled; (3) an estimation of the critical supersaturation required to form the droplets sampled; and (4) a prediction of the critical diameter for activation of rBC cores. Steps 1–3 are required to carry out the predictions in step 4.

3.7.1 Bulk aerosol composition

A HR-Tof-AMS was used to measure the bulk aerosol composition downstream of the CVI. Five species (organic, nitrate, sulfate, ammonium and chloride) were quantitatively differentiated. Then, based on a simplified ion-pairing scheme similar to Gysel and

ACPD
14, 11447–11491, 2014

Crosier (2007) (see Appendix B), the mass fractions of ammonium nitrate, ammonium sulfate, ammonium bisulfate, sulfuric acid, and ammonium chloride were calculated. The results of these calculations are shown in Fig. 8. In order to determine the bulk aerosol hygroscopicity (see Eq. 3), mass fractions, of these individual components, were first converted to volume fractions using an organic density of 1.4 g cm^{-3} (Moore et al., 2012) and densities reported in Lide (2001) for the inorganic salts.

3.7.2 The critical diameter for activation of the bulk aerosol in the cloud droplets sampled

The critical diameter for activation (D_{crit}) of the bulk aerosol is often calculated by integrating the residual number distribution from the largest to the smallest diameters until the number concentration equals the CDNC sampled (see for example Hersey et al., 2013). Using this method, D_{crit} was found to be 241 nm and 239 nm for Cloud 2 and Cloud 3 respectively. Note these D_{crit} apply only to the cloud droplets sampled (i.e. cloud droplets $>\approx$11 µm). Different D_{crit} values would be expected if the entire droplet population were sampled.

3.7.3 Critical supersaturation for the cloud droplets sampled

To estimate the critical supersaturation (S_C) for the formation of cloud droplets sampled during the two cloud events (i.e. cloud droplets $>\approx$11 µm) the single parameter kappa-Köhler model (Petters and Kreidenweis, 2007) was used. This model describes the relationship between the water vapor saturation ratio (S) over an aqueous solution droplet, and can be calculated using the following equation:

$$S = \frac{D^3 - D_p^3}{D^3 - D_p^3(1-\kappa_{Bulk})} \exp\left(\frac{4\sigma M_w}{\rho_w R T D}\right), \quad (2)$$

where D is the droplet diameter; D_p is the dry particle diameter; σ is the droplet surface tension, and is assumed to be that of water, 0.072 J m^{-2}; M_w is the molecular weight of

ACPD
14, 11447–11491, 2014

water; ρ_w is the density of water; R is the universal gas constant; T is the temperature; and κ_{Bulk} is a compositionally specific parameter that describes the bulk aerosol's hygroscopicity. Equation (2) was used to find S_C needed for a particle of dry diameter D_p to activate (Petters and Kreidenweis, 2007).

The overall hygroscopicity of a particular aerosol follows a simple mixing rule and can be calculated from:

$$\kappa_{Bulk} = \sum_i \epsilon_i \kappa_i, \quad (3)$$

where ϵ_i is the volume fraction and κ_i is the hygroscopicity parameter for each component i discussed in Sect. 3.7.1. The individual κ values used in Eq. (3) were; 0.1 for organic (Lance et al., 2013; Moore et al., 2012; Rose et al., 2010); 0.67 for ammonium nitrate (Petters and Kreidenweis, 2007); 0.61 for ammonium sulfate and ammonium bisulfate (Petters and Kreidenweis, 2007; Wu et al., 2013); and 0.71 for sulfuric acid, which is the average of the range reported in Shantz et al. (2008). The value for ammonium chloride κ was calculated according to Eq. (A28) in Rose et al. (2008) using a Van't Hoff factor of 2.

Using the above κ_i values and the values for ϵ_i, discussed in Sect. 3.7.1, in Eq. (3), κ_{Bulk} values of 0.50 and 0.41 were calculated for Cloud 2 and Cloud 3 respectively. The values determined during this study are consistent with the values suggested by Andreae and Rosenfeld (2008) for Cloud 2 and lower than the values suggested for Cloud 3.

Shown in Fig. 9a are plots of S_C as a function of dry diameter for Cloud 2 (solid line) and Cloud 3 (dashed line) calculated using Eqs. (2) and (3). Combining D_{crit} (see Sect. 3.7.2) with the results plotted in Fig. 9, S_C for the cloud droplets sampled can be determined. The points at which D_{crit} intersects with the calculated S_C traces shown in Fig. 9, result in estimations of S_C values of 0.05 % for both clouds. Note, these S_C apply only to the droplets sampled by the CVI. Different S_C values would be expected if the entire droplet population had been sampled.

ACPD
14, 11447–11491, 2014

In this determination of S_C several assumptions were made, which are addressed separately below: (1) the predominant mechanism for incorporation of particles into droplets was nucleation scavenging, and influences by impaction were negligible (Noone et al., 1992); (2) the contribution from sea salt aerosols could be neglected. Based on sea salt mass concentrations measured by the HR-Tof-AMS behind the CVI and calibrated against collocated ion chromotography measurements following a procedure similar to that introduced by Ovadnevaite et al. (2012), we estimated an upper limit of approximately 15 % for the sea salt mass fraction of cloud residuals (these results will be discussed in detail in a future publication). A sensitivity study (not shown here) indicated a < 8 % decrease in the estimated S_C values when a sea salt fraction of 15 % was included; (3) we assumed that the particles were internally mixed and the composition did not depend on size. Since, during this study, the size dependent AMS data were at or below the detection limit we could not determine if the composition was dependent on size. Additionally, no measurements of the bulk aerosol mixing state were carried out; and (4) we assumed that the entire fraction of organics was water soluble and represented by a κ of 0.1. To determine if S_C was sensitive to this value, κ for organics was varied from 0–0.2, which is roughly consistent with the range of κ values reported in the literature for organics (Chang et al., 2010; Lathem et al., 2013; Mei et al., 2013). Over this range of κ values, S_C varied by < 4 %.

3.7.4 Predictions of the critical diameter for activation of rBC cores

In Fig. 9b the critical diameter for activation of rBC cores, for cloud droplets sampled, is calculated using kappa-Köhler theory and assuming coating thicknesses ranging from 0–200 nm, which covers the range of coating thicknesses measured. In these calculations the composition of the coating was assumed to be the same as determined by the AMS (see Sect. 3.7.1), and the rBC cores were assumed to be insoluble with a $\kappa = 0$ (Rose et al., 2010). As expected, in Fig. 9b, S_C decreases as the coating thickness increases at a constant rBC core diameter. Figure 9b also shows that if the S_C is $> \approx 0.05$ %, for both clouds, the critical diameter for activation of the rBC cores is

ACPD
14, 11447–11491, 2014

< 50 nm for all cores with coating ≥ 100 nm. This quantitative prediction is consistent with rBC cores of 100 nm and less being activated into the sampled cloud droplets.

4 Summary and conclusions

Cloud residuals were measured during two cloud events at the top of Mt. Soledad in La Jolla, CA. Back trajectories showed that air masses for both cloud events spent at least 96 h over the Pacific Ocean and traveled near, or over populated regions before arriving on site. Based on measured bulk aerosol number concentrations the two air masses sampled were classified as polluted marine air, a classification that was consistent with the back trajectories and measured concentrations of black carbon mass.

The size distributions of the bulk aerosol residuals were shifted to larger sizes for both cloud events compared to the size distributions measured from the total inlet. The size distributions of rBC cloud residuals were also shifted towards larger diameters when compared to the size distributions of rBC measured from the total inlet. The measurements of the cloud residuals clearly show that rBC cores less than 100 nm can be incorporated into cloud droplets and therefore contribute to the CCN population. The activated fraction of 70–80 nm rBC cores was 0.01 and 0.045 for Cloud 2 and Cloud 3 respectively. Since the fraction of cloud droplets sampled by the CVI was less than 100 %, the measured activated fractions of rBC are lower limits to the total fraction of rBC activated during these two cloud events. The coating analysis of the SP2 data shows that the rBC cores that were activated into cloud droplets had thick coatings, with average coating thicknesses of ≈ 75 nm at core diameters between 70–80 nm and ≈ 29 nm coatings for core diameters between 200–210 nm. Furthermore, the presence of rBC cores less than 100 nm in cloud residuals is consistent with kappa-Köhler theory and the measured rBC coating thicknesses.

ACPD
14, 11447–11491, 2014

Appendix A

Procedure for calculating CVI – D_{50}

The CVI – D_{50} is the minimum droplet diameter for which the stopping distance (D_{stop}) is greater than the combination of CVI probe size and the distance between the CVI inlet and the internal stagnation plane (L_{stag}) and can be calculated based on the following equation:

$$\text{CVI} - D_{50} = D_{stop} > L_{stag} \tag{A1}$$

where L_{stag} is comprised of three components, and is equal to:

$$L_{stag} = L_{min} + L_{por} + L_{cur} \tag{A2}$$

where L_{min} is the amount of dead-space that exists between the CVI orifice and the top of the porous frit, L_{por} is the length from the top of the porous frit to the bottom of the stagnation plane, which is related to the counterflow ($F1$), sample flow ($F2$), and the length of the entire porous frit (X) by Eq. (A3):

$$L_{por} = \left[\frac{F1 - F2}{F1}\right] X \tag{A3}$$

L_{cur} is a parameterization (Anderson et al., 1993) that estimates the length a particle must traverse to deviate from the high velocity streamlines curving around the CVI probe tip in order to enter the CVI orifice, and is considered a linear function of the outer radius (r_o) of the tip:

$$L_{cur} = C r_o \tag{A4}$$

where C can range from 0 to 1 (Noone et al., 1988; Anderson et al., 1993) and represents the uncertainty of the estimate. In this study, CVI – D_{50} was reported at $C = 0.5$

ACPD
14, 11447–11491, 2014

and the uncertainty was calculated by averaging the differences calculated when using the lower and upper bounds of $C = 0$ and $C = 1$, respectively.

D_{Stop} can be calculated as follows (Serafini, 1954):

$$D_{\mathrm{Stop}} = \frac{r_{\mathrm{d}}\rho_{\mathrm{d}}}{3\epsilon^{\frac{3}{2}}\rho_{\mathrm{air}}}\left[Re_{\mathrm{d}}^{\frac{1}{3}}\epsilon^{\frac{1}{2}} - \frac{\pi}{2} + \tan^{-1}\left(Re_{\mathrm{d}}^{-\frac{1}{3}}\epsilon^{-\frac{1}{2}}\right)\right] \quad \text{(A5)}$$

where r_{d} is the droplet radius, ρ_{d} is the droplet density, ϵ is a constant (0.158), ρ_{air} is the density of air, and Re_{d} is the droplet Reynolds number, which is represented by:

$$Re_{\mathrm{d}} = \frac{2\rho_{\mathrm{d}}r_{\mathrm{d}}V_{\infty}}{\eta_{\mathrm{air}}} \quad \text{(A6)}$$

where V_{∞} is the CVI air intake velocity, and η_{air} is the viscosity of air.

The calculation needed to determine the CVI enhancement factor (EF) is:

$$\mathrm{EF} = \frac{V_{\infty}\pi r_{\mathrm{i}}^2}{F2} \quad \text{(A7)}$$

where r_{i} is the inner radius of the CVI probe tip.

Appendix B

AMS ion pairing scheme

The inorganic ions (NH_4^+, NO_3^-, SO_4^{2-}, Cl^-) mass fractions measured with the HR-ToF-AMS were converted to mass fractions of ammonium nitrate, ammonium sulfate, ammonium bisulfate, sulfuric acid, or ammonium chloride using the simplified ion-pairing scheme below:

$$n_{NH_4NO_3} = n_{NO_3^-}$$

ACPD
14, 11447–11491, 2014

$$n_{NH_4Cl} = n_{Cl^-}$$

$$n_{(NH_4)_2SO_4} = \max(0, n_{NH_4^+} - n_{SO_4^{2-}} - n_{NO_3^-} - n_{Cl^-})$$

$$n_{NH_4HSO_4} = \min(2n_{SO_4^{2-}} - n_{NH_4^+} + n_{NO_3^-} + n_{Cl^-}, n_{NH_4^+} - n_{NO_3^-} - n_{Cl^-})$$

$$n_{H_2SO_4} = \max(0, n_{SO_4^{2-}} - n_{NH_4^+} + n_{NO_3^-} + n_{Cl^-})$$

Where n is the number of moles of that species. This ion scheme is the same as the one used by Gysel and Crosier (2007) except it has been modified to incorporate ammonium chloride.

Appendix C

Determination of the droplet transmission in the the CVI

The droplet transmission factor (DT) through the CVI was determined by plotting the number of droplets measured by the FM-100 that were greater than the CVI – D_{50} as a function of the number of residual particles (see Fig. A1). The number of residual particles plotted in Fig. A1 were corrected for the CVI enhancement factor (EF) and only residual particles > 100 nm were included since particles smaller than this size were likely not due to nucleation scavenging (see Sect. 3.3.2 for further discussion). From 1/slope in Fig. A1a and b, the DT values were determined to be 26 % during Cloud 2 and 45 % during Cloud 3. DT values less than 100 % may be attributed to ; (1) particle or droplet losses in the CVI; (2) incomplete drying of the droplets; (3) misalignment of droplets in the wind tunnel prior to entering the CVI; and (4) insufficient acceleration of some of the larger droplets.

Acknowledgements. The authors would like to thank D. Toom-Sauntry, S. Sharma, and A. Sheppard, from Environment Canada, as well as A. Lee, and R. Zhou, from the University of Toronto, for their contributions during the campaign. The authors are also grateful for fund-

ACPD
14, 11447–11491, 2014

ing provided by Environment Canada through the Clean Air Regulatory Agenda, NSERC, NSF (grant AGS1013423), and the FORMAS MACCII project.

References

Allan, J. D., Delia, A. E., Coe, H., Bower, K. N., Alfarra, M., Jimenez, J. L., Middlebrook, A. M., Drewnick, F., Onasch, T. B., Canagaratna, M. R., Jayne, J. T., and Worsnop, D. R.: A generalised method for the extraction of chemically resolved mass spectra from Aerodyne aerosol mass spectrometer data, J. Aerosol Sci., 35, 909–922, doi:10.1016/j.jaerosci.2004.02.007, 2004. 11456

Anderson, T. L., Charlson, R. J., and Covert, S.: Calibration of a counterflow virtual impactor at aerodynamic diameters from 1 to 15 µm, Aerosol Sci. Tech., 19, 37–41, 1993. 11452, 11468

Andreae, M. O.: Correlation between cloud condensation nuclei concentration and aerosol optical thickness in remote and polluted regions, Atmos. Chem. Phys., 9, 543–556, doi:10.5194/acp-9-543-2009, 2009. 11460

Andreae, M. and Rosenfeld, D.: Aerosol–cloud–precipitation interactions. Part 1. The nature and sources of cloud-active aerosols, Earth-Sci. Rev., 89, 13–41, 2008. 11465

Bates, T. S., Quinn, P. K., Covert, D. S., Coffman, D. J., Johnson, J. E., and Wiedensohler, A.: Aerosol physical properties and processes in the lower marine boundary layer: a comparison of shipboard sub-micron data from ACE-1 and ACE-2, Tellus B, 52, 258–272, 2000. 11460

Bates, T. S., Coffman, D. J., Covert, D. S., and Quinn, P. K.: Regional marine boundary layer aerosol size distributions in the Indian, Atlantic, and Pacific Oceans: a comparison of INDOEX measurements with ACE-1, ACE-2, and Aerosols99, J. Geophys. Res., 107, 8026, doi:10.1029/2001JD001174, 2002. 11451

Bond, T. C. and Bergstrom, R. W.: Light absorption by carbonaceous particles: an investigative review, Aerosol Sci. Tech., 40, 27–67, 2006. 11453, 11455

Bond, T. C., Doherty, S. J., Fahey, D. W., Forster, P. M., Berntsen, T., DeAngelo, B. J., Flanner, M. G., Ghan, S., Kärcher, B., Koch, D., Kinne, S., Kondo, Y., Quinn, P. K., Sarofim, M. C., Schultz, M. G., Schulz, M., Venkataraman, C., Zhang, H., Zhang, S., Bellouin, N., Guttikunda, S. K., Hopke, P. K., Jacobson, M. Z., Kaiser, J. W., Klimont, Z., Lohmann, U., Schwarz, J. P., Shindell, D., Storelvmo, T., Warren, S. G., and Zender, C. S.: Bounding the

ACPD
14, 11447–11491, 2014

role of black carbon in the climate system: a scientific assessment, J. Geophys. Res.-Atmos., 118, 5380–5552, 2013. 11449

Chang, R. Y.-W., Slowik, J. G., Shantz, N. C., Vlasenko, A., Liggio, J., Sjostedt, S. J., Leaitch, W. R., and Abbatt, J. P. D.: The hygroscopicity parameter (κ) of ambient organic aerosol at a field site subject to biogenic and anthropogenic influences: relationship to degree of aerosol oxidation, Atmos. Chem. Phys., 10, 5047–5064, doi:10.5194/acp-10-5047-2010, 2010. 11466

Chen, W., Lee, Y. H., Adams, P. J., Nenes, A., and Seinfeld, J. H.: Will black carbon mitigation dampen aerosol indirect forcing?, Geophys. Res. Lett., 37, L09801, doi:10.1029/2010GL042886, 2010. 11450

Ching, J., Riemer, N., and West, M.: Impacts of black carbon mixing state on black carbon nucleation scavenging: insights from a particle-resolved model, J. Geophys. Res., 117, D23209, doi:10.1029/2012JD018269, 2012. 11449

Cooke, W.: Black carbon measurements at Mace Head, 1989–1996, J. Geophys. Res., 102, 1989–1996, 1997. 11460

Cozic, J., Verheggen, B., Mertes, S., Connolly, P., Bower, K., Petzold, A., Baltensperger, U., and Weingartner, E.: Scavenging of black carbon in mixed phase clouds at the high alpine site Jungfraujoch, Atmos. Chem. Phys., 7, 1797–1807, doi:10.5194/acp-7-1797-2007, 2007. 11449, 11450, 11458

DeCarlo, P. and Kimmel, J.: Field-deployable, high-resolution, time-of-flight aerosol mass spectrometer, Anal. Chem., 78, 8281–8289, 2006. 11456

Draxler, R. R. and Rolph, G. D.: HYSPLIT (HYbrid Single-Particle Langrangian Integrated Trajectory) Model access via NOAA ARL READY website (http://ready.arl.noaa.gov/HYSPLIT.php), NOAA Air Resources Laboratory, Silver Spring, MD., 2013. 11456

Dusek, U., Frank, G. P., Massling, A., Zeromskiene, K., Iinuma, Y., Schmid, O., Helas, G., Hennig, T., Wiedensohler, A., and Andreae, M. O.: Water uptake by biomass burning aerosol at sub- and supersaturated conditions: closure studies and implications for the role of organics, Atmos. Chem. Phys., 11, 9519–9532, doi:10.5194/acp-11-9519-2011, 2011. 11449

Eugster, W., Burkard, R., Holwerda, F., Scatena, F. N., and Bruijnzeel, L.: Characteristics of fog and fogwater fluxes in a Puerto Rican elfin cloud forest, Agr. Forest Meteorol., 139, 288–306, 2006. 11457

Gao, R. S., Schwarz, J. P., Kelly, K. K., Fahey, D. W., Watts, L. A., Thompson, T. L., Spackman, J. R., Slowik, J. G., Cross, E. S., Han, J. H., Davidovits, P., Onasch, T. B., and

ACPD
14, 11447–11491, 2014

Worsnop, D. R.: A novel method for estimating light-scattering properties of soot aerosols using a modified single-particle soot photometer, Aerosol Sci. Tech., 41, 125–135, 2007. 11454, 11455

Glantz, P. and Noone, K. J.: A physically-based algorithm for estimating the relationship between aerosol mass and cloud droplet number, Tellus B, 52, 1216–1231, 2000. 11460

Granat, L., Engström, J. E., Praveen, S., and Rodhe, H.: Light absorbing material (soot) in rainwater and in aerosol particles in the Maldives, J. Geophys. Res., 115, 1–12, 2010. 11450

Gysel, M., Crosier, J., Topping, D. O., Whitehead, J. D., Bower, K. N., Cubison, M. J., Williams, P. I., Flynn, M. J., McFiggans, G. B., and Coe, H.: Closure study between chemical composition and hygroscopic growth of aerosol particles during TORCH2, Atmos. Chem. Phys., 7, 6131–6144, doi:10.5194/acp-7-6131-2007, 2007. 11463, 11470

Gysel, M., Laborde, M., Olfert, J. S., Subramanian, R., and Gröhn, A. J.: Effective density of Aquadag and fullerene soot black carbon reference materials used for SP2 calibration, Atmos. Meas. Tech., 4, 2851–2858, doi:10.5194/amt-4-2851-2011, 2011. 11453

Hallberg, A., Ogren, J., and Noone, K.: Phase partitioning for different aerosol species in fog, Tellus B, 44, 545–555, 1992. 11449, 11450

Hallberg, A., Ogren, J., Noone, K., Okada, K., Heintzenberg, J., and Svenningsson, I.: The influence of aerosol particle composition on cloud droplet formation, J. Atmos. Chem., 19, 153–171, 1994. 11449, 11450, 11462

Hawkins, L. N., Russell, L. M., Covert, D. S., Quinn, P. K., and Bates, T. S.: Carboxylic acids, sulfates, and organosulfates in processed continental organic aerosol over the southeast Pacific Ocean during VOCALS-REx 2008, J. Geophys. Res., 115, D13201, doi:10.1029/2009JD013276, 2010. 11460

Henning, S., Wex, H., Hennig, T., Kiselev, A., Snider, J. R., Rose, D., Dusek, U., Frank, G. P., Pöschl, U., Kristensson, A., Bilde, M., Tillmann, R., Kiendler-Scharr, A., Mentel, T. F., Walter, S., Schneider, J., Wennrich, C., and Stratmann, F.: Soluble mass, hygroscopic growth, and droplet activation of coated soot particles during LACIS Experiment in November (LExNo), J. Geophys. Res., 115, D11206, doi:10.1029/2009JD012626, 2010. 11449, 11450

Henning, S., Ziese, M., Kiselev, A., Saathoff, H., Möhler, O., Mentel, T. F., Buchholz, A., Spindler, C., Michaud, V., Monier, M., Sellegri, K., and Stratmann, F.: Hygroscopic growth and droplet activation of soot particles: uncoated, succinic or sulfuric acid coated, Atmos. Chem. Phys., 12, 4525–4537, doi:10.5194/acp-12-4525-2012, 2012. 11449, 11450

ACPD
14, 11447–11491, 2014

Hersey, S. P., Craven, J. S., Metcalf, A. R., Lin, J., Lathem, T., Suski, K. J., Cahill, J. F., Duong, H. T., Sorooshian, A., Jonsson, H. H., Shiraiwa, M., Zuend, A., Nenes, A., Prather, K. A., Flagan, R. C., and Seinfeld, J. H.: Composition and hygroscopicity of the Los Angeles aerosol: CalNex, J. Geophys. Res.-Atmos., 118, 3016–3036, 2013. 11464

Hitzenberger, R., Berner, A., Kromp, R., Kasper-Giebl, A., Limbeck, A., Tscherwenka, W., and Puxbaum, H.: Black carbon and other species at a high-elevation European site (Mount Sonnblick, 3106 m, Austria): concentrations and scavenging efficiencies, J. Geophys. Res., 105, 24637–24645, 2000. 11449, 11450

Hitzenberger, R., Berner, A., Glebl, H., Drobesch, K., Kasper-Giebl, A., Loeflund, M., Urban, H., and Puxbaum, H.: Black carbon (BC) in alpine aerosols and cloud water – concentrations and scavenging efficiencies, Atmos. Environ., 35, 5135–5141, 2001. 11449, 11450

Jacobson, M. Z.: Investigating cloud absorption effects: global absorption properties of black carbon, tar balls, and soil dust in clouds and aerosols, J. Geophys. Res., 117, D06205, doi:10.1029/2011JD017218, 2012. 11449

Kasper-Giebl, A., Koch, A., Hitzenberger, R., and Puxbaum, H.: Scavenging efficiency of "aerosol carbon" and sulfate in soopercooled clouds at Mount Sonnblick (3106 m a.s.l., Austria), J. Atmos. Chem., 35, 33–46, 2000. 11449, 11450

Koch, D., Balkanski, Y., Bauer, S. E., Easter, R. C., Ferrachat, S., Ghan, S. J., Hoose, C., Iversen, T., Kirkevåg, A., Kristjansson, J. E., Liu, X., Lohmann, U., Menon, S., Quaas, J., Schulz, M., Seland, Ø., Takemura, T., and Yan, N.: Soot microphysical effects on liquid clouds, a multi-model investigation, Atmos. Chem. Phys., 11, 1051–1064, doi:10.5194/acp-11-1051-2011, 2011. 11449

Koehler, K. A., DeMott, P. J., Kreidenweis, S. M., Popovicheva, O. B., Petters, M. D., Carrico, C. M., Kireeva, E. D., Khokhlova, T. D., and Shonija, N. K.: Cloud condensation nuclei and ice nucleation activity of hydrophobic and hydrophilic soot particles, Phys. Chem. Chem. Phys., 11, 7906–7920, 2009. 11449

Kuwata, M., Kondo, Y., and Takegawa, N.: Critical condensed mass for activation of black carbon as cloud condensation nuclei in Tokyo, J. Geophys. Res., 114, D20202, doi:10.1029/2009jd012086, 2009. 11449

Lance, S., Raatikainen, T., Onasch, T. B., Worsnop, D. R., Yu, X.-Y., Alexander, M. L., Stolzenburg, M. R., McMurry, P. H., Smith, J. N., and Nenes, A.: Aerosol mixing state, hygroscopic growth and cloud activation efficiency during MIRAGE 2006, Atmos. Chem. Phys., 13, 5049–5062, doi:10.5194/acp-13-5049-2013, 2013. 11465

ACPD
14, 11447–11491, 2014

Lathem, T. L., Beyersdorf, A. J., Thornhill, K. L., Winstead, E. L., Cubison, M. J., Hecobian, A., Jimenez, J. L., Weber, R. J., Anderson, B. E., and Nenes, A.: Analysis of CCN activity of Arctic aerosol and Canadian biomass burning during summer 2008, Atmos. Chem. Phys., 13, 2735–2756, doi:10.5194/acp-13-2735-2013, 2013. 11466

Lide, D. R. (Ed.): CRC Handbook of Chemistry and Physics, 82nd Edn., CRC Press, Boca Raton, Florida, 2001. 11464

Mätzler, C.: MATLAB Functions for Mie Scattering and Absorption Version 1 – Research Report No. 2002-08, Univercity of Bern, 2002a. 11454

Mätzler, C.: MATLAB Functions for Mie Scattering and Absorption Version 2 – Research Report No. 2002-11, Univercity of Bern, 2002b. 11454

Mei, F., Hayes, P. L., Ortega, A., Taylor, J. W., Allan, J. D., Gilman, J., Kuster, W., de Gouw, J., Jimenez, J. L., and Wang, J.: Droplet activation properties of organic aerosols observed at an urban site during CalNex-LA, J. Geophys. Res.-Atmos., 118, 2903–2917, 2013. 11466

Metcalf, A. R., Craven, J. S., Ensberg, J. J., Brioude, J., Angevine, W., Sorooshian, A., Duong, H. T., Jonsson, H. H., Flagan, R. C., and Seinfeld, J. H.: Black carbon aerosol over the Los Angeles Basin during CalNex, J. Geophys. Res.-Atmos., 117, D00V13, doi:10.1029/2011jd017255, 2012. 11449, 11455, 11460, 11462

Moore, R. H., Cerully, K., Bahreini, R., Brock, C. A., Middlebrook, A. M., and Nenes, A.: Hygroscopicity and composition of California CCN during summer 2010, J. Geophys. Res.-Atmos., 117, D00V12, doi:10.1029/2011JD017352, 2012. 11464, 11465

Moteki, N. and Kondo, Y.: Method to measure time-dependent scattering cross sections of particles evaporating in a laser beam, J. Aerosol Sci., 39, 348–364, 2007. 11453

Moteki, N., Kondo, Y., Takegawa, N., and Nakamura, S.-I.: Directional dependence of thermal emission from nonspherical carbon particles, J. Aerosol Sci., 40, 790–801, 2009. 11453

Noone, K. J., Ogren, J. A., Heintzenberg, J., Charlson, R. J., and Covert, D. S.: Design and calibration of a counterflow virtual impactor for sampling of atmospheric fog and cloud droplets, Aerosol Sci. Tech., 8, 235–244, 1988. 11452, 11468

Noone, K. J., Ogren, J. A., Hallberg, A., Heintzenberg, J., Ström, J., Hansson, H.-C., Svenningsson, B., Wiedensohler, A., Facchinni, M. C., Arends, B. G., and Berner, A.: Changes in aerosol-size- and phase distributions due to physical and chemical processes in fog, Tellus B, 44, 489–504, 1992. 11449, 11466

O'Dowd, C., Becker, E., and Kulmala, M.: Mid-latitude North-Atlantic aerosol characteristics in clean and polluted air, Atmos. Res., 58, 167–185, 2001. 11460

ACPD
14, 11447–11491, 2014

Ovadnevaite, J., Ceburnis, D., Canagaratna, M., Berresheim, H., Bialek, J., Martucci, G., Worsnop, D. R., and O'Dowd, C.: On the effect of wind speed on submicron sea salt mass concentrations and source fluxes, J. Geophys. Res., 117, D16201, doi:10.1029/2011JD017379, 2012. 11466

Pekour, M. and Cziczo, D.: Wake capture, particle breakup, and other artifacts associated with counterflow virtual impaction, Aerosol Sci. Tech., 45, 37–41, 2011. 11461

Petters, M. D. and Kreidenweis, S. M.: A single parameter representation of hygroscopic growth and cloud condensation nucleus activity, Atmos. Chem. Phys., 7, 1961–1971, doi:10.5194/acp-7-1961-2007, 2007. 11464, 11465

Petters, M. D., Carrico, C. M., Kreidenweis, S. M., Prenni, A. J., DeMott, P. J., Collett, J. L., and Moosmüller, H.: Cloud condensation nucleation activity of biomass burning aerosol, J. Geophys. Res., 114, D22205, doi:10.1029/2009JD012353, 2009. 11449

Petzold, A., Gysel, M., Vancassel, X., Hitzenberger, R., Puxbaum, H., Vrochticky, S., Weingartner, E., Baltensperger, U., and Mirabel, P.: On the effects of organic matter and sulphur-containing compounds on the CCN activation of combustion particles, Atmos. Chem. Phys., 5, 3187–3203, doi:10.5194/acp-5-3187-2005, 2005. 11449, 11450

Pirjola, L. and O'Dowd, C.: Can new particle formation occur in the clean marine boundary layer?, J. Geophys. Res., 105, 26531–26546, 2000. 11460

Popovicheva, O. B., Persiantseva, N. M., Kireeva, E. D., Khokhlova, T. D., and Shonija, N. K.: Quantification of the hygroscopic effect of soot aging in the atmosphere: laboratory simulations., J. Phys. Chem. A, 115, 298–306, 2011. 11449, 11450

Riemer, N., Vogel, H., and Vogel, B.: Soot aging time scales in polluted regions during day and night, Atmos. Chem. Phys., 4, 1885–1893, doi:10.5194/acp-4-1885-2004, 2004. 11449

Riemer, N., West, M., Zaveri, R., and Easter, R.: Estimating black carbon aging time-scales with a particle-resolved aerosol model, J. Aerosol Sci., 41, 143–158, 2010. 11449

Rolph, G. D.: Real-time Environmental Application and Display sYstem (READY) website (http://ready.arl.noaa.gov), NOAA Air Resources Laboratory, Silver Spring, MD, 2013. 11456

Rose, D., Gunthe, S. S., Mikhailov, E., Frank, G. P., Dusek, U., Andreae, M. O., and Pöschl, U.: Calibration and measurement uncertainties of a continuous-flow cloud condensation nuclei counter (DMT-CCNC): CCN activation of ammonium sulfate and sodium chloride aerosol particles in theory and experiment, Atmos. Chem. Phys., 8, 1153–1179, doi:10.5194/acp-8-1153-2008, 2008. 11465

ACPD
14, 11447–11491, 2014

Rose, D., Nowak, A., Achtert, P., Wiedensohler, A., Hu, M., Shao, M., Zhang, Y., Andreae, M. O., and Pöschl, U.: Cloud condensation nuclei in polluted air and biomass burning smoke near the mega-city Guangzhou, China – Part 1: Size-resolved measurements and implications for the modeling of aerosol particle hygroscopicity and CCN activity, Atmos. Chem. Phys., 10, 3365–3383, doi:10.5194/acp-10-3365-2010, 2010. 11465, 11466

Schwarz, J. P., Gao, R. S., Fahey, D. W., Thomson, D. S., Watts, L. A., Wilson, J. C., Reeves, J. M., Darbeheshti, M., Baumgardner, D. G., Kok, G. L., Chung, S. H., Schulz, M., Hendricks, J., Lauer, A., Kärcher, B., Slowik, J. G., Rosenlof, K. H., Thompson, T. L., Langford, A. O., Loewenstein, M., and Aikin, K. C.: Single-particle measurements of midlatitude black carbon and light-scattering aerosols from the boundary layer to the lower stratosphere, J. Geophys. Res., 111, 1–15, 2006. 11453

Schwarz, J. P., Gao, R. S., Spackman, J. R., Watts, L. A., Thomson, D. S., Fahey, D. W., Ryerson, T. B., Peischl, J., Holloway, J. S., Trainer, M., Frost, G. J., Baynard, T., Lack, D. A., de Gouw, J. A., Warneke, C., and Del Negro, L. A.: Measurement of the mixing state, mass, and optical size of individual black carbon particles in urban and biomass burning emissions, Geophys. Res. Lett., 35, L13810, doi:10.1029/2008GL033968, 2008a. 11455, 11462

Schwarz, J. P., Spackman, J. R., Fahey, D. W., Gao, R. S., Lohmann, U., Stier, P., Watts, L. A., Thomson, D. S., Lack, D. A., Pfister, L., Mahoney, M. J., Baumgardner, D., Wilson, J. C., and Reeves, J. M.: Coatings and their enhancement of black carbon light absorption in the tropical atmosphere, J. Geophys. Res., 113, 1–10, 2008b. 11449, 11454, 11455

Schwarzenboeck, A., Heintzenberg, J., and Mertes, S.: Incorporation of aerosol particles between 25 and 850 nm into cloud elements: measurements with a new complementary sampling system, Atmos. Res., 52, 241–260, 2000. 11461

Sedlacek, A. J., Lewis, E. R., Kleinman, L., Xu, J., and Zhang, Q.: Determination of and evidence for non-core-shell structure of particles containing black carbon using the Single-Particle Soot Photometer (SP2), Geophys. Res. Lett., 39, L06802, doi:10.1029/2012GL050905, 2012. 11462

Sellegri, K., Laj, P., Dupuy, R., Legrand, M., Preunkert, S., and Putaud, J.: Size-dependent scavenging efficiencies of multicomponent atmospheric aerosols in clouds, J. Geophys. Res., 108, 2156–2202, 2003. 11449, 11450

Serafini, J. S.: Impingement of water droplets on wedges and double-wedge airfoils at supersonic speeds, TR 1159, NACA, Washington, 1954. 11469

ACPD
14, 11447–11491, 2014

Shank, L. M., Howell, S., Clarke, A. D., Freitag, S., Brekhovskikh, V., Kapustin, V., McNaughton, C., Campos, T., and Wood, R.: Organic matter and non-refractory aerosol over the remote Southeast Pacific: oceanic and combustion sources, Atmos. Chem. Phys., 12, 557–576, doi:10.5194/acp-12-557-2012, 2012. 11460

Shantz, N. C., Leaitch, W. R., Phinney, L., Mozurkewich, M., and Toom-Sauntry, D.: The effect of organic compounds on the growth rate of cloud droplets in marine and forest settings, Atmos. Chem. Phys., 8, 5869–5887, doi:10.5194/acp-8-5869-2008, 2008. 11465

Stephens, M., Turner, N., and Sandberg, J.: Particle identification by laser-induced incandescence in a solid-state laser cavity., Appl. Optics, 42, 3726–36, 2003. 11453

Twohy, C., Petters, M., and Snider, J.: Evaluation of the aerosol indirect effect in marine stratocumulus clouds: droplet number, size, liquid water path, and radiative impact, J. Geophys. Res., 110, 1–16, 2005. 11460

Verheggen, B., Cozic, J., Weingartner, E., Bower, K., Mertes, S., Connolly, P., Gallagher, M., Flynn, M., Choularton, T., and Baltensperger, U.: Aerosol partitioning between the interstitial and the condensed phase in mixed-phase clouds, J. Geophys. Res., 112, 1–13, 2007. 11449, 11450

Vidaurre, G., Hallett, J., and Rogers, D. C.: Airborne measurement of liquid and total water content, J. Atmos. Ocean. Tech., 28, 1088–1103, 2011. 11461

Vignati, E., Karl, M., Krol, M., Wilson, J., Stier, P., and Cavalli, F.: Sources of uncertainties in modelling black carbon at the global scale, Atmos. Chem. Phys., 10, 2595–2611, doi:10.5194/acp-10-2595-2010, 2010. 11449

von der Weiden, S.-L., Drewnick, F., and Borrmann, S.: Particle Loss Calculator – a new software tool for the assessment of the performance of aerosol inlet systems, Atmos. Meas. Tech., 2, 479–494, doi:10.5194/amt-2-479-2009, 2009. 11452

Wang, C.: Impact of anthropogenic absorbing aerosols on clouds and precipitation: a review of recent progresses, Atmos. Res., 122, 237–249, 2013. 11449

Wang, Z., Zhang, H., Li, J., Jing, X., and Lu, P.: Radiative forcing and climate response due to the presence of black carbon in cloud droplets, J. Geophys. Res.-Atmos., 118, 1–14, 2013. 11449

Wu, Z. J., Poulain, L., Henning, S., Dieckmann, K., Birmili, W., Merkel, M., van Pinxteren, D., Spindler, G., Müller, K., Stratmann, F., Herrmann, H., and Wiedensohler, A.: Relating particle hygroscopicity and CCN activity to chemical composition during the HCCT-2010 field campaign, Atmos. Chem. Phys., 13, 7983–7996, doi:10.5194/acp-13-7983-2013, 2013. 11465

ACPD
14, 11447–11491, 2014

Zhao, R., Lee, A., Liggio, J., Wentzall, J., Macdonald, A., Toom-Sauntry, D., Leaitch, W., Modini, R., Corrigan, A., Russell, L., Noone, K., Schroder, J., Bertram, A., Hawkins, L., and Abbatt, J.: Cloud Scavenging of Isocyanic Acid (HNCO) and evidence of a secondary source of HNCO in ambient air, Geophys. Res. Lett., in review, 2014. 11452

Zhuang, B. L., Liu, L., Shen, F. H., Wang, T. J., and Han, Y.: Semidirect radiative forcing of internal mixed black carbon cloud droplet and its regional climatic effect over China, J. Geophys. Res., 115, D00K19, doi:10.1029/2009JD013165, 2010. 11449

ACPD
14, 11447–11491, 2014

Table 1. Summary of cloud microphysical properties showing the average CVI cut-size (CVI – D_{50}) where the uncertainty stems from the calculated cut-size (see text for details); average liquid water content (LWC) and one standard deviation; and the cloud droplet number ($CDNC_{Tot}$) and volume (Vol_{Tot}) concentrations for droplets with diameters between 2–50 µm. Also shown is the number $\left(\frac{CDNC_{Samp}}{CDNC_{Tot}}\right)$ and volume $\left(\frac{Vol_{Samp}}{Vol_{Tot}}\right)$ fractions of droplets sampled, where $CDNC_{Samp}$ and Vol_{Samp} are the number and volume concentrations, respectively, for the fraction of droplets sampled.

Cloud #	Date Sampled	CVI – D_{50} (µm)	LWC ($g\,m^{-3}$)	$CDNC_{Tot}$ (cm^{-3})	$\left(\frac{CDNC_{Samp}}{CDNC_{Tot}}\right)$	Vol_{Tot} ($\mu m^3\,m^{-3}$)	$\left(\frac{Vol_{Samp}}{Vol_{Tot}}\right)$
2	12–13 Jun 2012 20:43–11:35 PDT	11.5 ±0.72	0.13 ±0.07	67.67	0.38	1.24×10^5	0.91
3	17–18 Jun 2012 20:36–07:52 PDT	11.6 ±0.72	0.09 ±0.02	145.8	0.24	8.88×10^4	0.68

ACPD
14, 11447–11491, 2014

Table 2. Averaged number (N) and mass (M) concentrations, modal parameters D_g and σ_g for aerosol and rBC particles during the two cloud events measured at Mt. Soledad. The subscripts Tot and Res represent measurements made from the total and residual inlets respectively.

	Cloud 2		Cloud 3	
	Aerosol	rBC	Aerosol	rBC
N_{Tot} (cm^{-3})	980.8	75.24	994.0	62.13
M_{Tot} ($ng\,m^{-3}$)	–	73.41	–	61.83
$D_{g,Tot}$ (nm)	107.7	< 0.07	80.54	< 0.07
$\sigma_{g,Tot}$	1.577	–	1.703	–
N_{Res} (cm^{-3})	43.46	2.000	83.15	3.86
M_{Res} ($ng\,m^{-3}$)	–	2.741	–	4.735
$D_{g,Res}$ (nm)	331.9	87.30	269.2	80.72
$\sigma_{g,Res}$	1.187	1.259	1.281	1.268

ACPD
14, 11447–11491, 2014

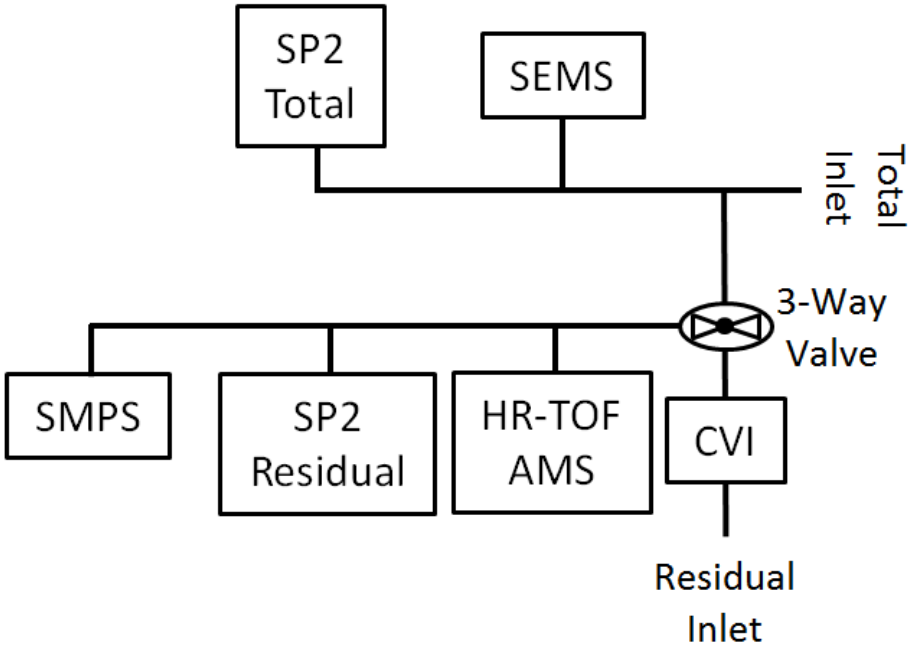

Fig. 1. Schematic showing the configuration of the inlets and instrumentation housed in the shipping container.

ACPD
14, 11447–11491, 2014

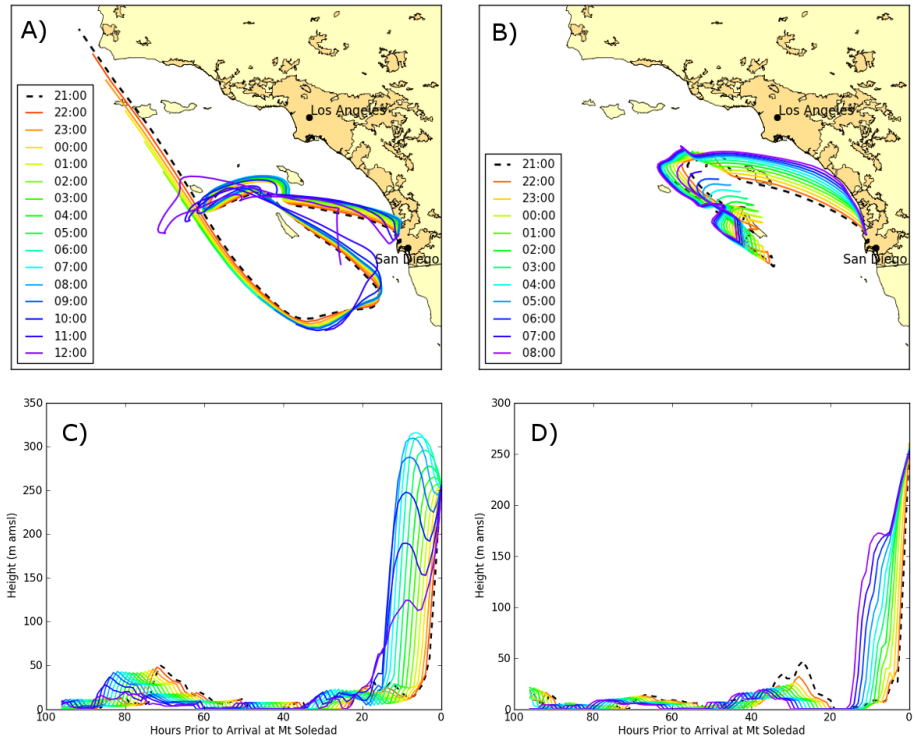

Fig. 2. In-cloud HYSPLIT 96 h back trajectories ending at hourly intervals for Cloud 2 (12 June 21:00 to 13 June 12:00 PDT) in (**A** and **C**), and Cloud 3 (17 June 21:00 to 18 June 08:00 PDT) in (**B** and **D**). All back trajectories started at 10 m a.g.l. Darker yellow regions on land in (**A** and **B**) indicate densely developed urban areas containing 50 000 or more people (United States Census Bureau). (**C** and **D**) show the vertical profiles over the same hourly intervals shown in (**A** and **B**).

ACPD
14, 11447–11491, 2014

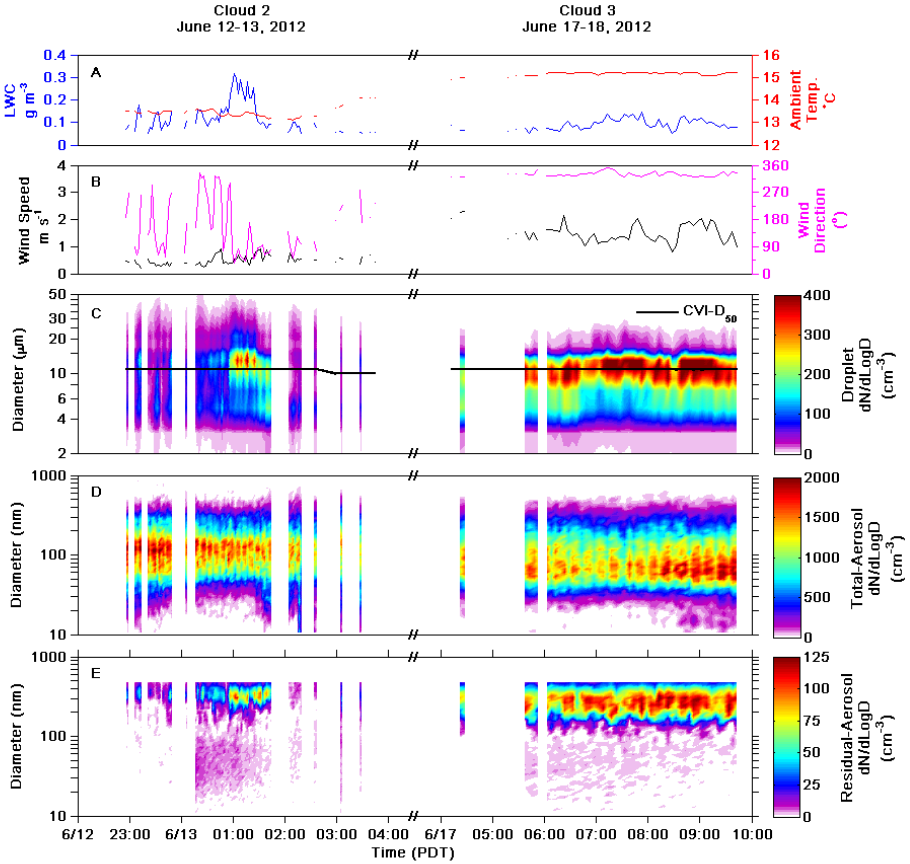

Fig. 3. Time series data for both Cloud 2 (left side) and Cloud 3 (right side) showing; liquid water content (LWC, blue trace) and ambient temperature (red trace) in **(A)**; wind speed and direction in **(B)**; cloud droplet number size distributions with the CVI – D_{50} (black trace) overlaid in **(C)**; the number size distribution for the total aerosol in **(D)**, and the residual aerosol in **(E)**. All data shown are five minute averages and meet the criteria discussed in the text.

ACPD
14, 11447–11491, 2014

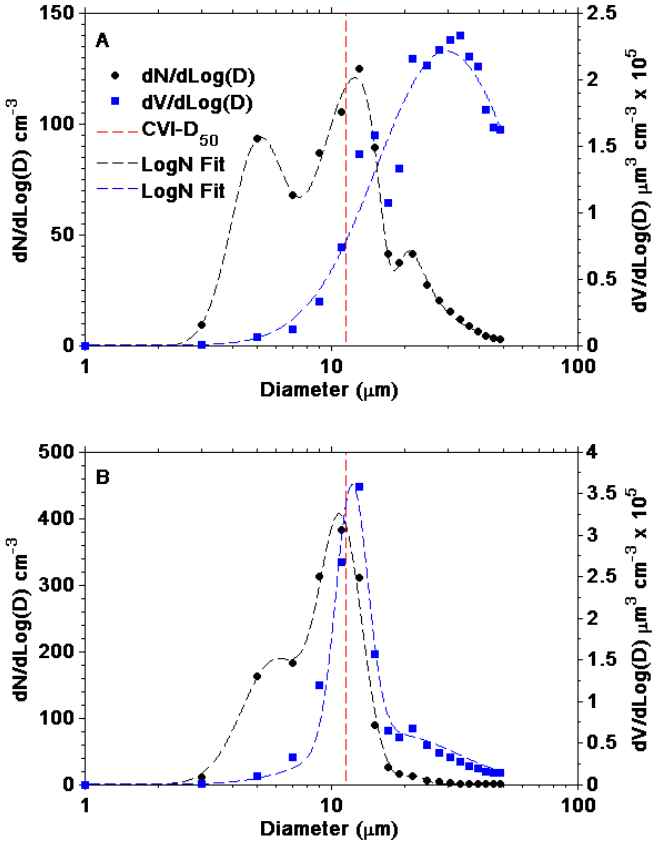

Fig. 4. Average cloud droplet number size distributions for Cloud 2 **(A)** and Cloud 3 **(B)** measured by the FM-100 (black circles) and fit to a lognormal distribution function (black dashed lines). The average cloud droplet volume distributions (blue squares) and lognormal fits (blue dashed lines) are also shown for each cloud event. The CVI – D_{50} is indicated on each panel by a red dashed line.

ACPD
14, 11447–11491, 2014

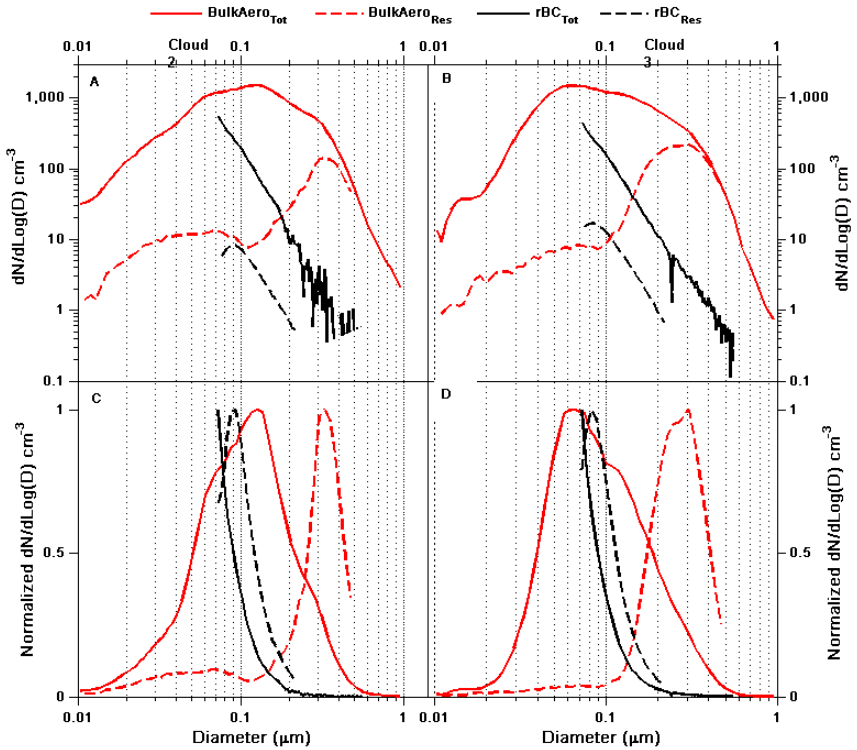

Fig. 5. Summary of the averaged number size distributions for Cloud 2 (**A** and **C**) and Cloud 3 (**B** and **D**) for the total aerosol (red solid lines); residual aerosol (red dashed lines); total rBC as a function of core diameter (black solid lines); residual rBC as a function of core diameter (black dashed lines). Both the aerosol and rBC for each cloud event are shown in two ways, a log scale (**A** and **B**) to highlight the relative differences between the aerosol and rBC as well as normalized to the respective maximum value (**C** and **D**) to highlight the shift in size distributions. All residual distributions have been corrected for CVI enhancement (see Appendix A) and droplet losses (see Appendix C).

ACPD
14, 11447–11491, 2014

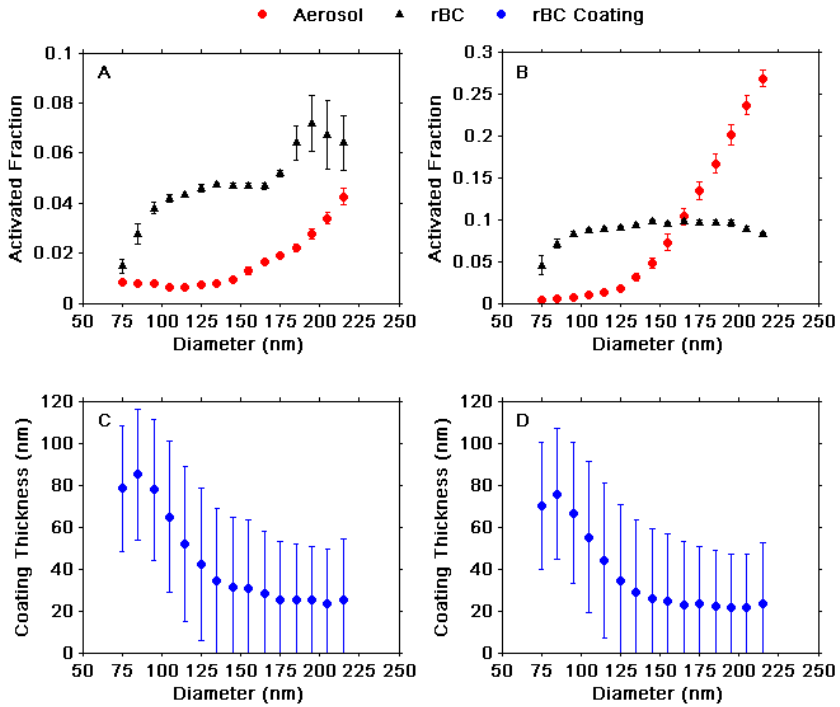

Fig. 6. Shown in (**A** and **B**) are the mean size dependent activated fraction (AF) for the aerosol (red circles), and rBC (black triangles) for Clouds 2 and 3, respectively, where the error bars represent one standard deviation (1σ) of the mean AF. The bottom axes represent particle diameter for the aerosol and core diameter for rBC. Since the fraction of the cloud droplets sampled by the CVI was less than 100 %, the calculated activated fractions should be considered as lower limits to the total activated fraction during the two cloud events. Shown in (**C** and **D**) are the averaged rBC coating thicknesses (blue circle) in nm with 1σ as the error bars. Since only 50 % of the rBC containing particles detected with the $SP2_{Res}$ were successfully fit with the LEO fitting procedure, the coating thicknesses shown in (**C** and **D**) are only from a subset (50 %) of the rBC particles measured with the $SP2_{Res}$.

ACPD
14, 11447–11491, 2014

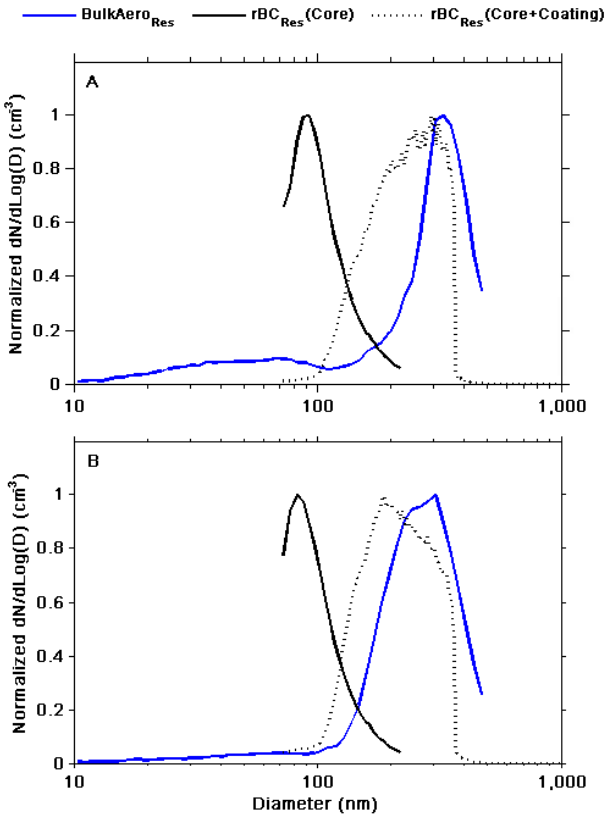

Fig. 7. Normalized number size distributions from Cloud 2 **(A)** and Cloud 3 **(B)** for residual rBC as a function of particle diameter [rBC$_{Res}$(Core+Coating)]. The residual bulk aerosol distribution (BulkAero$_{Res}$) and rBC distribution as a function of core diameter [rBC$_{Res}$(Core)] are also shown for comparison. Since only 50 % of the rBC containing particles detected with the SP2$_{Res}$ were successfully fit with the LEO fitting procedure, the rBC$_{Res}$(Core + Coating) shown in (**A** and **B**) are only from a subset (50 %) of the rBC particles measured with the SP2$_{Res}$.

ACPD
14, 11447–11491, 2014

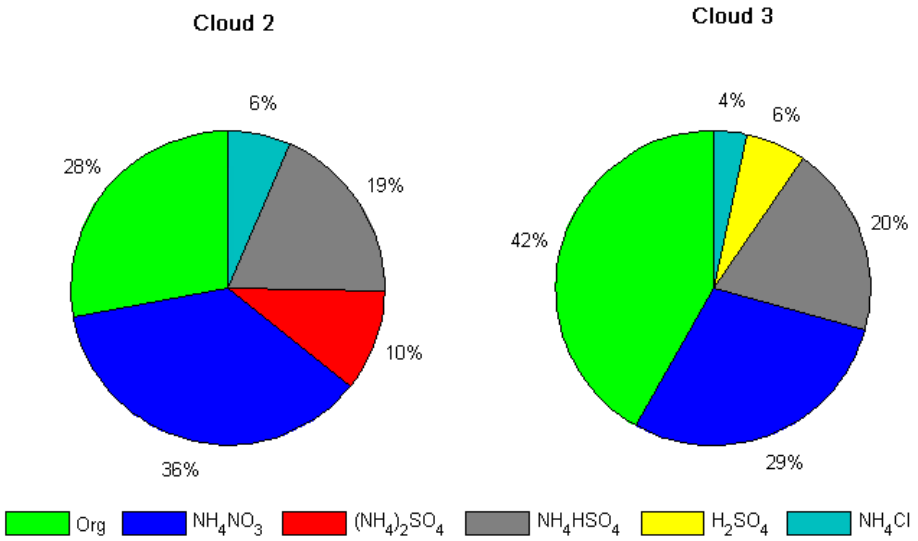

Fig. 8. Sub-micrometer non-refractory average aerosol mass fractions for Clouds 2 and 3 based on an ion-pairing scheme (see text and Appendix B) and measured from a high resolution time-of-flight aerosol mass spectrometer.

ACPD
14, 11447–11491, 2014

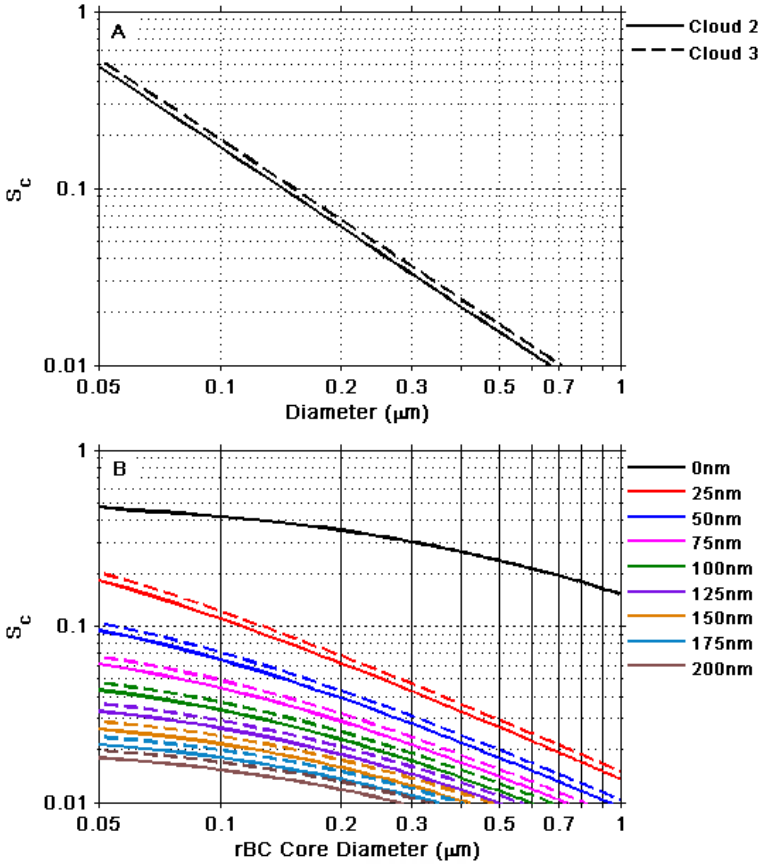

Fig. 9. (A) shows the critical supersaturation (S_C, black lines) as a function of particle dry diameter based on measured AMS bulk compositions and an ion-pairing scheme. **(B)** shows S_C as a function of rBC core diameters with coatings ranging from 0–200 nm. In **(B)**, the coatings are assumed to have the same composition as the bulk residual aerosol (Fig. 8). The solid lines are for Cloud 2 and the dashed lines are for Cloud 3.

ACPD
14, 11447–11491, 2014

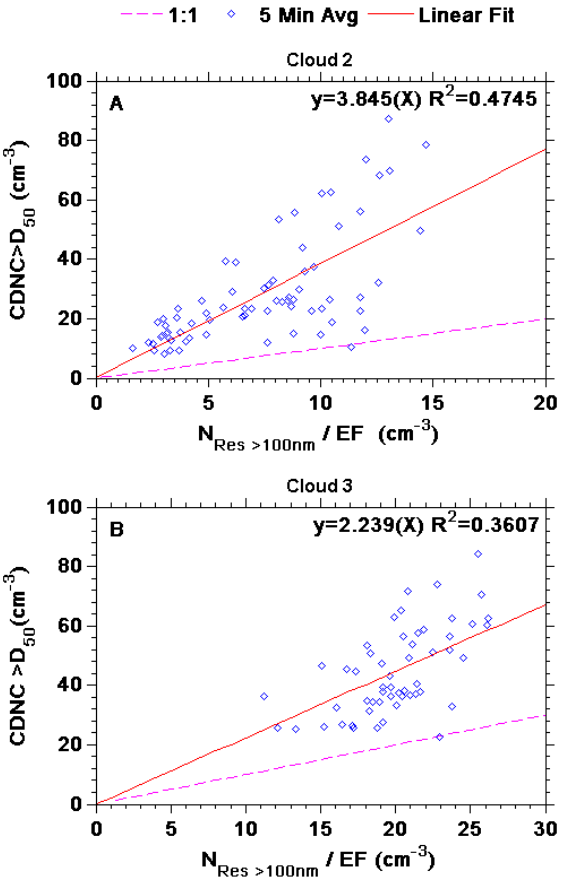

Fig. A1. Correlation plots between the cloud droplet number concentration (CDNC) greater than the CVI – D_{50} (CDNC > D_{50}) and the enhancement factor (EF) corrected residual number concentration greater than 100 nm ($N_{\mathrm{Res>100\,nm}}$) in cm^{-3}.

ACPD
14, 11447–11491, 2014